Volume 3 | Number 14 | 14 April 2015 | Pages 3227–3502

Journal of Materials Chemistry C

Materials for optical, magnetic and electronic devices

www.rsc.org/MaterialsC

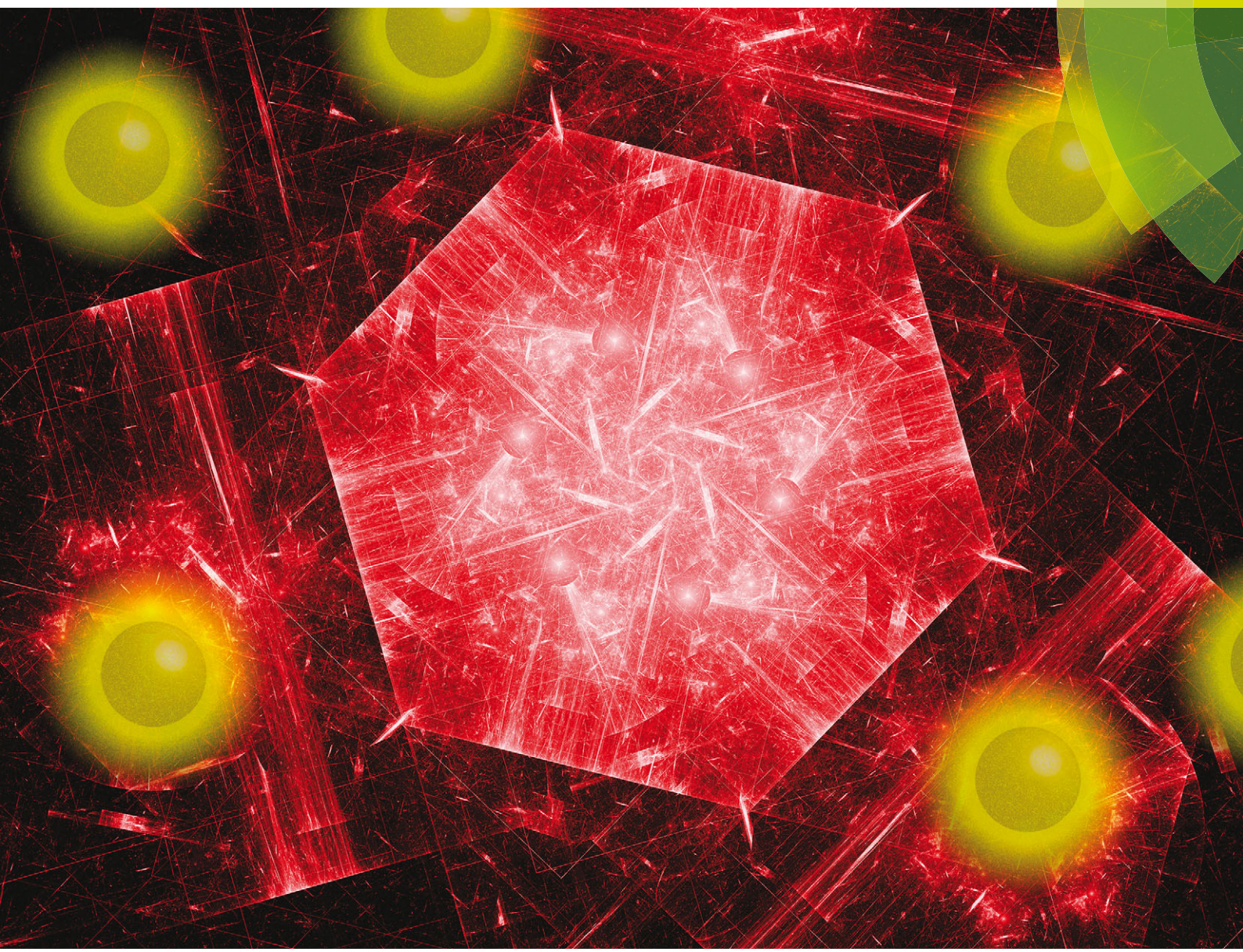

ISSN 2050-7526

ROYAL SOCIETY OF CHEMISTRY

PAPER

J. E. Macdonald *et al.*

Phase dependent visible to near-infrared photoluminescence of $CuInS_2$ nanocrystals

Journal of Materials Chemistry C

PAPER

View Article Online
View Journal | View Issue

Cite this: J. Mater. Chem. C, 2015, 3, 3258

Phase dependent visible to near-infrared photoluminescence of $CuInS_2$ nanocrystals†

A. D. P. Leach, L. G. Mast, E. A. Hernández-Pagán and J. E. Macdonald*

Received 14th January 2015,
Accepted 6th February 2015

DOI: 10.1039/c5tc00134j

www.rsc.org/MaterialsC

Nanocrystals of $CuInS_2$ with the hexagonal wurtzite structure hold great potential for applications requiring efficient energy transport, such as photocatalysis, due to their anisotropic crystal structure. However, thus far their optical properties have proven difficult to study, as luminescence from wurtzite nanocrystals has only recently been observed. In this work, we report the colloidal synthesis of single crystalline, luminescent $CuInS_2$ nanocrystals with both the cubic and hexagonal structures. The crystalline phase, optical properties and mechanism of formation of nanocrystals are controlled by changing the reaction temperature. Photoluminescence is observed in the visible and near-infrared spectral regions, which results from the cubic and hexagonal nanocrystals respectively. Synthetic studies combined with XRD, TEM and EDS mapping provide evidence for the mechanisms behind phase selection.

Introduction

Semiconductor nanocrystals (NCs) have garnered significant attention from the scientific community due to their tuneable, size-dependent opto-electronic properties and large surface area.[1,2] These properties give rise to many potential applications, including use in photovoltaic devices,[3] biological sensing,[4] as catalysts,[5] and photocatalysts.[6] Amongst the most commonly studied semiconductor NC systems are the II–VI cadmium chalcogenides.[7,8] However, currently these systems are not optimal as the toxicity of Cd leads to concerns about disposal of NC containing devices and limits *in vivo* use.[9] Further they suffer from photoinstability under the conditions used for water splitting, restricting their use as photocatalysts.[10,11] Therefore NC systems with different constituent elements, but similar opto-electronic properties are sought.

Copper indium sulfide ($CuInS_2$) is a particularly promising alternative to the cadmium chalcogenide systems, due to the lower toxicity of its constituent elements and its high photostability.[12] Further, the material has a direct band gap $\sim$1.5 eV in magnitude,[13] ideally energetically situated for water reduction, and a large optical absorption coefficient ($\alpha > 10^5$ cm^{-1}).[14] NCs of $CuInS_2$ have also shown unexpected phases not observed in the bulk, with nanocrystals reported in three distinct structures: chalcopyrite (CP), zinc blende (ZB), and wurtzite (WZ).[15,16] CP, the thermodynamic product seen in the bulk phase, is a tetragonal distortion of the cubic ZB phase. It is also the most commonly produced phase and therefore has been extensively studied.[17–20]

The hexagonal WZ structure of $CuInS_2$, only isolable thus far in nanostructures, is particularly interesting as it is anisotropic in the crystallographic *c*-direction.[21] The exploitation of this anisotropy will improve and control electronic, structural and chemical properties in light-absorbing technologies: the anisotropic electronic structure can be used for orthogonal charge propagation in solar cell or photocatalyst design;[22] the hexagonal crystal structure is being used to grow asymmetric nanocrystals,[23,24] which can act as light absorbing antennae;[25] the anisotropic surface chemistry can be used to enhance epitaxial interactions to an appropriate substrate and has been used to increase charge transfer rates in solar cell design, improving efficiencies.[26]

The WZ phase of $CuInS_2$ nanocrystals was first identified in 2008 by Pan *et al.*[27] Since then, WZ $CuInS_2$ NCs have been synthesized by a variety of methods with a range of accessible morphologies including plates, rods and spheres.[27–29] Fundamental studies on both cation ordering within the structure[30] and the electronic band structure of the material[31] have been undertaken. However, the luminescence properties of this material have not yet been completely elucidated, as few examples of luminescent WZ NCs have been reported and none synthesized *via* direct methods.[32]

The mechanism by which the WZ structure is preferentially formed in colloidal syntheses is not yet fully understood. Several groups have shown evidence of a hexagonal copper sulfide intermediate, possibly achieved through the decomposition of a copper thiolate complex.[23,27,33] Others have evoked the role of stronger metal coordinating agents controlling nucleation kinetics.[34,35]

Department of Chemistry and the Vanderbilt Institute of Nanoscale Science and Engineering, Vanderbilt University, Nashville, Tennessee, 37235, USA. E-mail: janet.macdonald@vanderbilt.edu

† Electronic supplementary information (ESI) available: Complete Rietveld refinement parameters; Scherrer line broadening crystallite size compared to TEM size; EDS data; quantum yields; Fityk peak fitting parameters; absorbance spectra of hexanes; TEM images from aliquot study; complete EDS maps for aliquot study, including dark field and elemental analysis data. See DOI: 10.1039/c5tc00134j

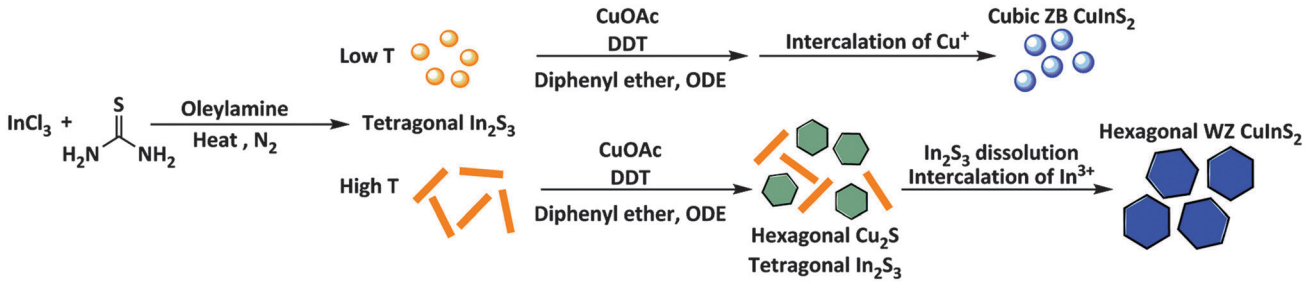

Fig. 1 Schematic illustration of the synthesis of $CuInS_2$ NCs.

Without complete understanding of the mechanism, the production of single crystalline, monodisperse, quantum confined WZ $CuInS_2$ remains a considerable challenge. Colloidal syntheses often instead yield polytypic NCs or hybrid particles composed of Cu_2S–In_2S_3 or Cu_2S–$CuInS_2$.[34,36–41]

In this paper, single crystalline NCs of $CuInS_2$ are prepared by a colloidal synthesis through the reaction of In_2S_3 NCs, formed *in situ*, with a Cu–thiolate complex (Fig. 1). By changing the reaction temperature, the crystalline phase, optical properties, and mechanism of formation of the product can be controlled. We propose that at low reaction temperature, cubic $CuInS_2$ is formed by the intercalation of Cu^+ ions into the tetragonal In_2S_3 intermediate. At higher reaction temperatures, the In_2S_3 acts only as an In^{3+} reservoir and WZ $CuInS_2$ NCs are formed by the intercalation of In^{3+} into a hexagonal Cu_2S intermediate. Two distinct regions of emission are observed in the photoluminescence (PL) spectra of these NCs. Emission in the visible region is assigned to ZB $CuInS_2$.[17,28,42,43] A broad peak in the near-infrared (NIR) is also observed and correlates to the presence of WZ $CuInS_2$ nanocrystals in the product.

This is the first report of WZ $CuInS_2$, produced using a direct synthesis, with emission in the near-infrared.[32] This will facilitate the study of these NCs through luminescence spectroscopies.[44–46] The complete understanding of this material's optical properties is key to the realization of its potential in photovoltaic and photocatalytic applications. Furthermore the observation of NIR PL within the tissue transparency window, from NCs with non-toxic constituent elements, shows the promise of WZ $CuInS_2$ for use in biological applications.

Experimental techniques

Materials

Indium chloride ($InCl_3$, Alfa Aesar, 99.99%), thiourea (Sigma-Aldrich, ≥99.0%), oleylamine (OlAm, Aldrich, 70%), copper(I) acetate (CuOAc, Strem Chemicals, 99%), 1-dodecanethiol (DDT, Aldrich, ≥98.0%), octadecene (ODE, Aldrich, 90%), diphenyl ether (Sigma-Aldrich, 99%) and *tert*-dodecylmercaptan (*t*-DDT, Aldrich, 98.5%) were purchased and used as received. Standard air-free Schlenk techniques were used throughout with N_2 as the inert gas.

Synthesis of $CuInS_2$ NCs

$CuInS_2$ NCs were prepared *via* the reaction scheme shown in Fig. 1. Briefly, $InCl_3$ (111.5 mg, 0.5 mmol) and thiourea (77.5 mg, 1.0 mmol) were added to oleylamine (10 mL) in the reaction vessel, degased for 1 h, and heated to the required temperature (115–235 °C) under a nitrogen atmosphere. Separately CuOAc (65.0 mg, 0.5 mmol) was suspended in ODE (500 μL), diphenyl ether (500 μL) and DDT (240 μL, 1.0 mmol). At the required reaction temperature, 1 mL of the Cu solution was injected quickly (<1 s) into the reaction vessel. After 30 min, the heat was removed and the reaction mixture was cooled to room temperature. The obtained $CuInS_2$ NCs were precipitated by addition of methanol–acetone (v/v, 2 : 1) and then purified by repeated centrifugation and decantation with addition of methanol–acetone and hexanes.

Transmission electron microscopy (TEM)

TEM images were collected and energy dispersive X-ray spectroscopy (EDS) was carried out using a FEI Tecnai Osiris™ digital 200 kV S/TEM system. TEM samples were prepared by drop casting a dilute NC solution in hexanes onto a nickel grid with a carbon support and drying in air at room temperature.

X-ray diffraction (XRD) and Rietveld refinement

XRD measurements were performed using a Scintag XGEN-4000 X-ray diffractometer with a CuKα (λ = 0.154 nm) radiation source. The resulting diffraction patterns were then visually compared to literature data to determine the structure.[36,47] Rietveld refinement was performed using the General Structure and Analysis System (GSAS) suite of programs and the EXPGUI interface.[48–50] The GSAS suite of programs allows the refinement of parameters including site occupancy, atomic parameters, lattice parameters, background coefficients, peak profiles, atomic displacements and preferred orientation. The quality of the refinement is monitored by visual comparison of calculated and observed patterns, facilitated by plotting a difference curve below the *X*-axis, and calculating the goodness-of-fit parameter, χ^2.

Optical spectroscopy

The absorption spectra of NC samples were collected from 300–1400 nm on a UV-visible spectrophotometer (Jasco V-670). Visible PL spectra were measured from 550–900 nm on a spectrofluorometer (Jasco FP-8300). NIR PL spectra were measured from 800–1400 nm on a different spectrofluorometer (Jobin Yvon/Horiba Fluorolog-3 FL3-111). Samples were measured in solution with hexanes as the solvent. Both visible and NIR PL were measured with excitation wavelength 348 nm. Data were then matched at 800 nm and normalized to the quantum yield (QY). The QY was determined for each sample by comparison to a

Rh-101 standard.[51] Finally data were analysed by using the Fityk application to fit Gaussian functions to emissive peaks.[52] The goodness of fit parameter, χ^2, was minimized *via* the Levenberg–Marquardt algorithm.

Results and discussion

Morphology of $CuInS_2$ NCs

TEM of the product NCs indicated that a variety of morphologies and NC sizes were accessible *via* this synthetic route (Fig. 2). At low temperature (115–135 °C) small, monodisperse, spherical particles (~1.5 nm in diameter) were observed that showed an increase in size at the higher temperature. When the reaction temperature was above 135 °C, rod- and plate-like products were seen in addition to the small spheres. Both these new morphologies showed increased size with increased reaction temperature, though the rods had a consistent width (1.8 nm). Further, the proportion of plates observed increased with reaction temperature.

Structure & composition of $CuInS_2$ NCs

In order to determine the structure of the prepared NCs XRD data were collected for each sample (Fig. 3a). For samples prepared at 115 °C, reflections characteristic of the ZB phase were observed. As the reaction temperature was increased, however, reflections characteristic of the WZ phase increased in intensity, appearing dominant for samples prepared at 215 °C and 235 °C. This structural trend was confirmed by Rietveld refinement of the resultant XRD patterns for each reaction temperature (Fig. 3b).

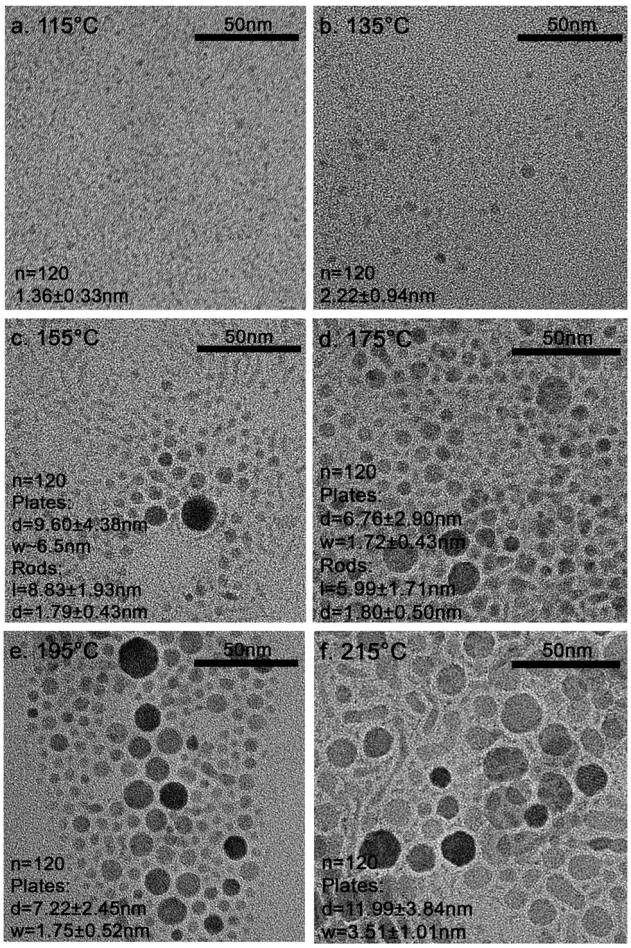

Fig. 2 (a)–(f) TEM images of $CuInS_2$ NCs prepared at reaction temperatures from 115–215 °C.

An EDS map collected from the sample prepared at 155 °C (Fig. 3c) indicated that some plate-shaped particles seen at intermediate temperatures consisted of only Cu and S. As a result the Rietveld refinement used to fit a structural model to the experimental data included three phases: the ZB and WZ $CuInS_2$ phases reported by Chang *et al.* and the high chalcocite copper sulfide (hiCC Cu_2S) phase reported by Wuensch *et al.*, (Fig. S1 and S2, ESI†).[36,47,50] For samples prepared at 115 °C and 135 °C, data were fit to within a statistically acceptable tolerance without the addition of the Cu_2S impurity phase (Fig. S2, ESI†).[53] Small amounts of WZ and hiCC Cu_2S may be present at these low reaction temperatures, however, crystallite size broadening of the more intense ZB peaks obscures the reflections from these phases.

Application of the Scherrer equation to the broadened peaks yielded NC domain sizes in good agreement to those of nanoplates (at high temperatures) and spheres (at low temperatures) measured by TEM for samples prepared below 235 °C (Fig. S3, ESI†). This suggests that the NCs are single crystalline, in contrast to many literature examples, which exhibit polytypism.[40,41] In order to ensure the prepared NCs were both single phase and single domain HRTEM images of individual NCs were collected. Lattice fringes in HRTEM show that the nanoplates (Fig. 3d) are single crystalline with a *d*-spacing of 0.34 nm indexed to the (100) plane of WZ $CuInS_2$.[28] In contrast, while the smaller spherical NCs (Fig. 3e) are also single crystalline, they have a *d*-spacing of 0.32 nm indexed to the (111) plane of ZB $CuInS_2$.[36]

Optical characterization of $CuInS_2$ NCs

The absorbance spectra for NC samples are shown in Fig. 4a. At lower reaction temperatures, the absorbance onset increases with increasing temperature, suggesting that the small NCs obtained at low reaction temperature are quantum confined. Above 175 °C, there is no significant change in absorbance onset, indicating that NCs have grown larger than the Wannier–Mott bulk exciton radius of $CuInS_2$ (~4 nm).[13] This is in good agreement with the average size of NCs, 7 ± 3 nm at 175 °C. A Tauc plot (Fig. 4b) was used to determine the band gap of the sample prepared at 215 °C, which consisted of >80% WZ phase NCs.[54,55] The calculated band gap of 1.56 eV was consistent with the literature value for the WZ phase, 1.55 eV.[30]

PL spectra were collected for all samples from 550–1400 nm and are shown in Fig. 4c normalized to the QY. Multiple emissive peaks can be observed in both the visible and NIR spectral regions. At low reaction temperatures, visible emission at ~640 nm is dominant, which has been previously reported for ZB $CuInS_2$, and is consistent with both TEM and XRD analysis.[17,42] At high reaction temperature only NIR emission is observed. It is attributed to WZ $CuInS_2$, the predominant

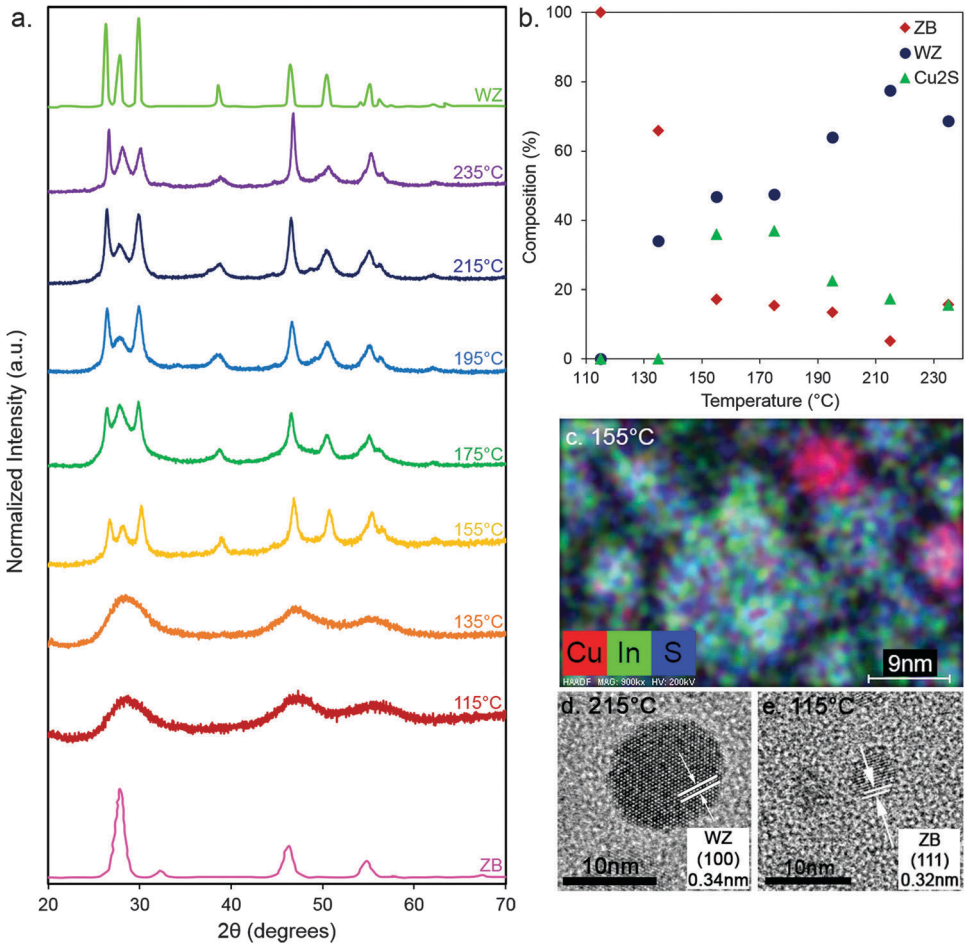

Fig. 3 (a) XRD of $CuInS_2$ NCs prepared at various temperatures. Pure ZB and WZ spectra are digitized from the work of Chang *et al.*;[36] (b) Proportion of WZ (blue), ZB (red) and hiCC Cu_2S (green) phases present in each sample plotted as a function of temperature, as determined by Rietveld refinement of XRD; (c) EDS map of $CuInS_2$ NCs prepared at 155 °C showing the presence of Cu_2S NCs; (d), (e) High resolution TEM (HRTEM) images of $CuInS_2$ NCs prepared at 215 °C (plates) and 115 °C (spheres) respectively showing lattice fringing.

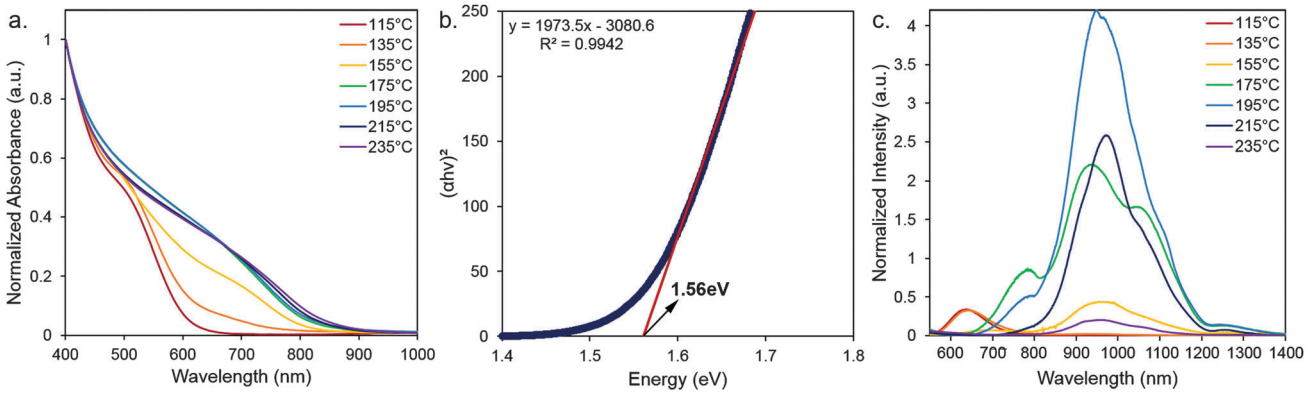

Fig. 4 (a) Absorbance spectra of $CuInS_2$ NC dispersions in hexanes prepared at different temperatures; (b) Tauc plot of the predominantly WZ $CuInS_2$ NCs prepared at 215 °C; (c) PL spectra normalized to the QY of $CuInS_2$ NC dispersions in hexanes prepared at different temperatures.

structure formed at these temperatures.[32] The QY was $<0.8\%$ for all samples (Fig. S5, ESI†).

The visible peak, attributed to ZB $CuInS_2$, was fit to a single Gaussian (Fig. S6, ESI†), which showed a red shift as reaction temperature increased. This is most likely due to an increase in the size of the NCs and the relaxation of quantum confinement conditions. This is consistent with the trends observed in absorbance spectra and reported in literature examples.[56–58]

The broad, multimodal shape of the NIR PL peak, centred at ~950 nm, and the large Stokes shift (0.25 eV) indicate that

emission is from several trap states. To identify the energetic location of specific emissive defects, spectra were fit using Fityk, a curve fitting and data analysis application.[52] The data were fit for all samples by four Gaussians centred at 810, 898, 969 and 1069 nm (Fig. S6, ESI†). A more detailed study of the origin and properties of this PL is currently being undertaken.

Mechanism of formation of prepared $CuInS_2$ NCs

In order to determine the mechanism of formation of the prepared $CuInS_2$ NCs, the In–S precursor solution, into which the Cu complex was injected, was examined. At 115 °C, TEM images collected (Fig. 5c) indicate that small, spherical NCs of In_2S_3 are formed with diameter 1.14 ± 0.36 nm. XRD measurements (Fig. 5a) indicate a tetragonal β-In_2S_3 phase (JCPDS card no. 25-0390) with considerable line broadening observed due to the small crystallite size.[59] EDS analysis showed that the NCs were S deficient with composition $In_2S_{2.5}$. The ZB $CuInS_2$ product of the complete reaction (Fig. 2) at 115 °C is of comparable size (1.36 ± 0.33 nm) to the In_2S_3 precursor and the crystal structures of the two materials are closely related (tetragonal to cubic). It is therefore likely that the ZB $CuInS_2$ product is formed by the intercalation of Cu^+ ions into the previously formed β-In_2S_3 NC host (Fig. 5c).[60]

At a reaction temperature of 215 °C, In_2S_3 NCs with rod-like morphology are observed with length 9.20 ± 5.88 nm and diameter 1.23 ± 0.44 nm (Fig. 5b). The resulting XRD pattern (Fig. 5a) was also indexed to the tetragonal phase, β-In_2S_3. The sharp (1 0 9) and (2 2 12) reflections suggest that rods are elongated in the *c*-direction.[61,62] Since the In_2S_3 is in the same phase at both reaction temperature extremes, it is unlikely that intercalation of Cu^+ into tetragonal In_2S_3 is also the mechanism by which the hexagonal WZ $CuInS_2$ is formed. Moreover, the morphology of the In_2S_3 precursor rods is very different than the $CuInS_2$ nanoplates. An alternative mechanism is needed to explain the formation of the distinct product crystal structure (WZ) at higher reaction temperature. Literature examples have shown that at reaction temperatures greater than 200 °C decomposition of a Cu–thiolate complex can occur yielding a Cu_2S intermediate.[63–67] It was hypothesized that the formation of the WZ $CuInS_2$ proceeds *via* this mechanism. To confirm the hypothesis, the chemistry of the injected Cu–DDT complex was altered.

At reaction temperature 115 °C, the DDT in the Cu solution was replaced by *tert*-dodecyl mercaptan (*t*-DDT). The tertiary carbon adjacent to the thiol in *t*-DDT facilitates the facile decomposition of the Cu–thiolate complex.[68] Therefore the injection of a Cu–*t*-DDT complex was expected to promote the nucleation of Cu_2S, leading to an increase in the proportion of WZ $CuInS_2$ formed at lower temperatures. XRD data of the NCs produced (Fig. 6a) indicated that indeed the dominant phase was WZ even at the low reaction temperature of 115 °C. TEM images (Fig. 6b) showed that the sample was polydisperse with plate-like morphology.

In an additional study, the DDT in the Cu solution was replaced by an equimolar amount of oleylamine (OlAm) at reaction temperature 215 °C. If the decomposition of the Cu–DDT complex causes the nucleation of hexagonal Cu_2S, allowing the growth of hexagonal WZ $CuInS_2$, the use of a Cu–amine complex should give only the ZB phase. The XRD pattern of the resulting NCs (Fig. 6a) was, as expected, indexed to the ZB phase of $CuInS_2$. TEM images (Fig. 6c) showed that these NCs had a mixture of morphologies with hexagonal and triangular shapes observed. Lattice fringing indicated that these morphologies were not

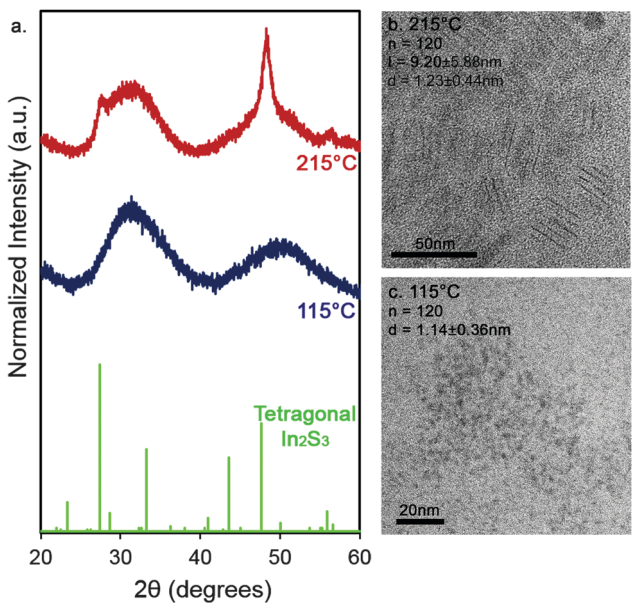

Fig. 5 (a) XRD patterns collected for In_2S_3 NCs prepared at 115 °C and 215 °C. Data for tetragonal β-In_2S_3 is from JCPDS card no. 25-0390; (b), (c) TEM images for precursor In_2S_3 NCs prepared at 215 °C and 115 °C respectively.

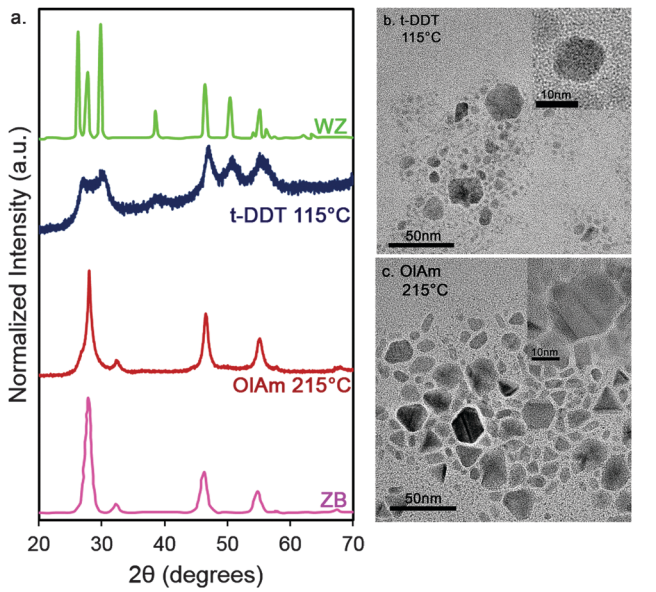

Fig. 6 (a) XRD patterns collected for $CuInS_2$ NCs prepared with OlAm as the injection solvent at 215 °C and *t*-DDT as the injection solvent at 115 °C. Pure ZB and WZ spectra are digitized from the work of Chang *et al.*;[36] (b), (c) TEM images collected for samples prepared with *t*-DDT injection at 115 °C and with OlAm injection at 215 °C respectively.

characteristic of a hexagonal phase, but of twinning of the cubic ZB phase. It is therefore clear that the mechanism of WZ formation proceeds *via* the decomposition of the Cu–thiolate complex.

To add further support to our mechanistic hypothesis, a detailed aliquot study of the reaction at 215 °C was undertaken. Six aliquots of the reaction mixture were taken every 15 s from injection of the Cu–DDT complex. The absorbance spectra of the aliquots (Fig. 7a) showed a steady increase with temperature in both onset and intensity at larger wavelength. This is indicative of both the size and proportion of WZ $CuInS_2$ increasing with time. PL measurements were also performed on each aliquot (Fig. 7b). Little fluorescence was observed at 15 s, suggesting that NCs are not yet completely crystalline, highly defective, or are in the non-fluorescent intermediate phases Cu_2S and In_2S_3.[39,69] As the reaction progressed a peak in the visible region was observed to grow over the first 30 s and then decayed completely by 30 min (Fig. 2). We have assigned PL in this region to ZB $CuInS_2$ and it is thought that this emission is due to some intercalation of Cu into previously formed β-In_2S_3. This observation suggests that the ZB $CuInS_2$ NCs are a reversible, kinetic product and WZ NCs are more stable at high reaction temperature. Continued heating caused the ZB NCs to dissolve in order for the growth of WZ particles to progress. This hypothesis is supported by the steady increase in intensity of PL in the NIR, which we have assigned to WZ $CuInS_2$.

Fig. 7c–e show EDS mapping data from aliquots taken at 15 s and 75 s, and 30 min. Bright field, dark field and elemental analysis images can be found in Fig. S8 and S9 (ESI†). After 15 s two distinct types of NC were present: nanoplates (diameter 7.40 ± 2.58 nm, depth 3.41 ± 0.53 nm), and nanorods (length 10.03 ± 4.67 nm, diameter 1.51 ± 0.39 nm). EDS mapping showed that the nanoplates were largely composed of Cu and S with some showing small amounts of In present. Lattice fringing in bright field TEM indicated that the nanoplates were single crystalline and had the hiCC Cu_2S structure (Fig. S8, ESI†).[38] Literature precedent suggests that the formation of these Cu_2S NCs was due to the decomposition of the Cu–thiolate complex into the Cu_2S intermediate.[63–67] The smaller rods were composed of In and S and were similar in size to the In_2S_3 rods (length 9.26 ± 1.23 nm, diameter 1.23 ± 0.44 nm) observed before injection.

As the reaction progressed, the nanoplates showed a small increase in size (diameter 7.40 ± 2.58 nm, depth 3.41 ± 0.53 nm at 15 s; and diameter 8.57 ± 2.68 nm, depth 3.60 ± 1.13 nm at 75 s). Further EDS mapping indicated that the proportion of In in the plates also increased with time (Fig. 7c–e). This suggests that the hiCC Cu_2S nanoplates are the most stable structure and early stage growth proceeds primarily through the intercalation of In into these NCs. The small In_2S_3 rods decreased in size with time and acted as a reservoir of In^{3+} ions. The large increase in WZ $CuInS_2$ nanoplate size between 75 s (Fig. S8, ESI†) and 30 min (Fig. 2) indicates that beyond the initial

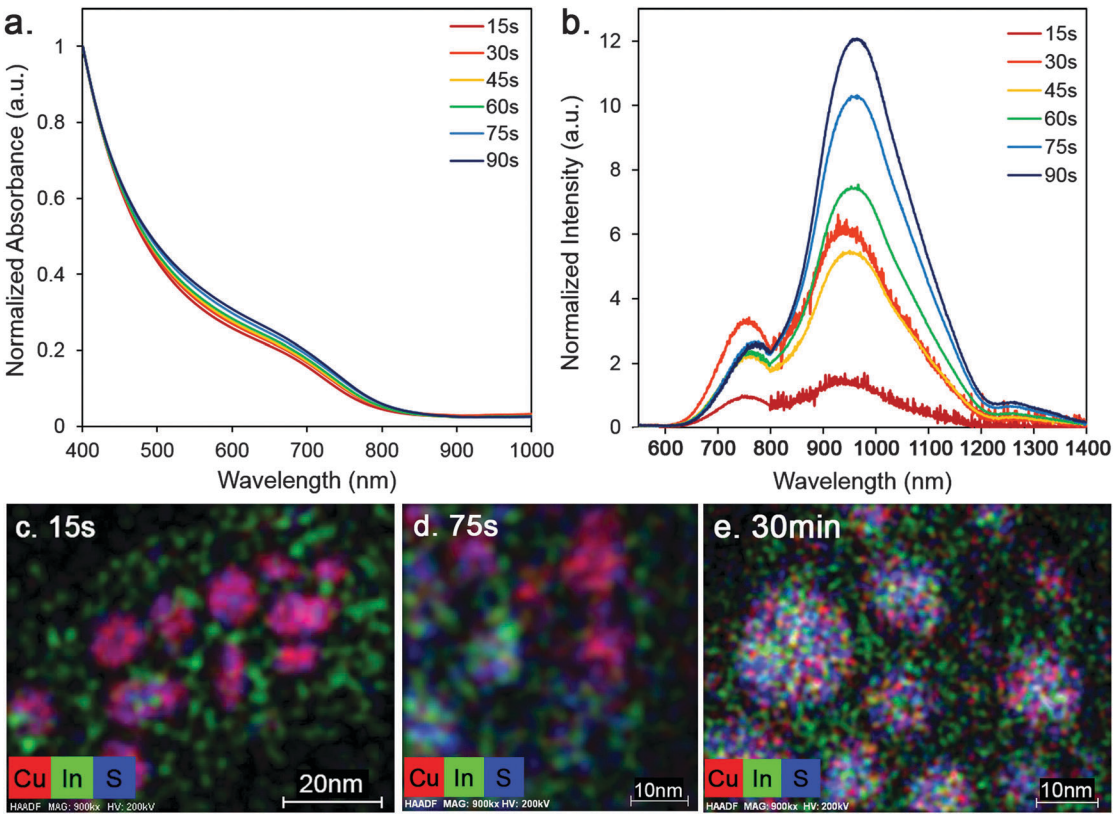

Fig. 7 (a) Absorbance and (b) PL spectra of aliquots taken from the synthesis of $CuInS_2$ NCs at 215 °C; (c), (d) EDS maps of the 15 s and 75 s aliquots taken from the synthesis of $CuInS_2$ NCs at 215 °C; (e) EDS map of the resultant $CuInS_2$ NCs produced by the synthesis for 30 min at 215 °C.

intercalation step, there is further growth through the addition of more reactant ions and/or Ostwald ripening processes.

In summary, the proposed mechanism of WZ $CuInS_2$ formation (Fig. 1) is as follows: on injection of the Cu–DDT complex, decomposition of the thiol causes the nucleation of hiCC Cu_2S. Then, as the reaction progresses, the dissolution of the precursor, In_2S_3 rods occurs. Excess In in the reaction mixture intercalates into the hiCC Cu_2S nanoplates forming WZ $CuInS_2$. Growth then proceeds until the reaction is quenched. This mechanism is in agreement with a number of literature examples, which report that the formation of WZ $CuInS_2$ occurs *via* a Cu_2S intermediate.[23,27,37] While not always explicitly implicated, in all of these examples a thiol is present in the reaction mixture and the reaction temperature is high enough ($\geq$200 °C) for the decomposition of a Cu–thiolate precursor to occur. Other studies suggest that WZ formation is dependent on the additional presence of a chelating amine ligand that coordinates strongly to the metallic precursors, manipulating the nucleation kinetics.[34,35] Reinterpretation with our experiments in mind, suggests that the amine chelates the In^{3+} and allows the formation of the Cu_2S intermediate necessary to WZ $CuInS_2$ formation.

Conclusions

A new synthetic method has been developed that produces WZ $CuInS_2$ nanoplates with broad emission in the NIR. Samples were multiphase (WZ and ZB) and the presence of both In_2S_3 and hiCC Cu_2S impurities was observed, however, by tuning the reaction temperature the relative proportion of these phases can be controlled. It was further found that the mechanism of WZ $CuInS_2$ NC formation proceeded *via* intercalation of In^{3+} into a hexagonal Cu_2S intermediate, while ZB $CuInS_2$ NCs were formed *via* intercalation of Cu^+ into tetragonal In_2S_3 precursor. Finally we determined that, in order to form the WZ structure, the decomposition of a Cu–thiolate precursor complex was necessary. Our mechanistic insight into the formation of this structure will inform future syntheses, advancing progress towards the production of quantum confined WZ $CuInS_2$ for solar energy capture.

This paper reports the first example of WZ $CuInS_2$ NCs, produced using a direct synthesis, with emission in the near-infrared that we are aware of. The observation of PL within the tissue transparency window, from NCs with non-toxic constituent elements, shows the exciting potential of WZ $CuInS_2$ for use in biological applications. Additionally the observation of PL provides a strong foundation for further study of the optical properties of $CuInS_2$ *via* luminescence spectroscopies. An understanding of these properties is indispensable in advancing work towards the use of this material in both photocatalytic and photovoltaic applications.

Acknowledgements

This material is based upon work supported by the National Science Foundation under CHE - 1253105, the US-Israel Binational Science Foundation-2012276, the Bergmann Memorial Research Award and the Arnold and Mabel Beckman Foundation's Beckman Scholars' Program. Portions of this work were performed at the Vanderbilt Institute of Nanoscale Science and Engineering, using facilities renovated under TN-SCORE (DMR 0907619) and NSF EPS-1004083.

Notes and references

1 M. A. El-Sayed, *Acc. Chem. Res.*, 2004, **37**, 326.
2 A. Eychmuller, *J. Phys. Chem. B*, 2000, **104**, 6514.
3 M. R. Kim, Z. Xu, G. Chen and D. Ma, *Chem. – Eur. J.*, 2014, **20**, 11256.
4 W. J. Parak, D. Gerion, T. Pellegrino, D. Zanchet, C. Micheel, S. C. Williams, R. Boudreau, M. A. Le Gros, C. A. Larabell and A. P. Alivisatos, *Nanotechnology*, 2003, **14**, R15.
5 L. L. Chng, N. Erathodiyil and J. Y. Ying, *Acc. Chem. Res.*, 2013, **46**, 1825.
6 A. Vaneski, J. Schneider, A. S. Susha and A. L. Rogach, *J. Photochem. Photobiol., C*, 2014, **19**, 52.
7 A. C. C. Esteves and T. Trindade, *Curr. Opin. Solid State Mater. Sci.*, 2002, **6**, 347.
8 N. V. Hullavarad, S. S. Hullavarad and P. C. Karulkar, *J. Nanosci. Nanotechnol.*, 2008, **8**, 3272.
9 B. A. Rzigalinski and J. S. Strobl, *Toxicol. Appl. Pharmacol.*, 2009, **238**, 280.
10 F. E. Osterloh, *Chem. Mater.*, 2008, **20**, 35.
11 A. Vaneski, A. S. Susha, J. Rodriguez-Fernandez, M. Berr, F. Jaeckel, J. Feldmann and A. L. Rogach, *Adv. Funct. Mater.*, 2011, **21**, 1547.
12 L. Li, T. J. Daou, I. Texier, C. Tran Thi Kim, L. Nguyen Quang and P. Reiss, *Chem. Mater.*, 2009, **21**, 2422.
13 J. Kolny-Olesiak and H. Weller, *ACS Appl. Mater. Interfaces*, 2013, **5**, 12221.
14 W. J. Yue, S. K. Han, R. X. Peng, W. Shen, H. W. Geng, F. Wu, S. W. Tao and M. T. Wang, *J. Mater. Chem.*, 2010, **20**, 7570.
15 X. T. Lu, Z. B. Zhuang, Q. Peng and Y. D. Li, *CrystEngComm*, 2011, **13**, 4039.
16 M. Booth, A. P. Brown, S. D. Evans and K. Critchley, *Chem. Mater.*, 2012, **24**, 2064.
17 H. Nakamura, W. Kato, M. Uehara, K. Nose, T. Omata, S. Otsuka-Yao-Matsuo, M. Miyazaki and H. Maeda, *Chem. Mater.*, 2006, **18**, 3330.
18 R. Klenk, J. Klaer, R. Scheer, M. C. Lux-Steiner, I. Luck, N. Meyer and U. Ruhle, *Thin Solid Films*, 2005, **480**, 509.
19 H. Zhong, S. S. Lo, T. Mirkovic, Y. Li, Y. Ding, Y. Li and G. D. Scholes, *ACS Nano*, 2010, **4**, 5253.
20 J. S. Niezgoda, M. A. Harrison, J. R. McBride and S. J. Rosenthal, *Chem. Mater.*, 2012, **24**, 3294.
21 X. Sheng, L. Wang, Y. P. Luo and D. R. Yang, *Nanoscale Res. Lett.*, 2011, **6**, 562.
22 P. R. Sajanlal, T. S. Sreeprasad, A. K. Samal and T. Pradeep, *Nano Rev.*, 2011, **2**, 5883.
23 J. Li, M. Bloemen, J. Parisi and J. Kolny-Olesiak, *ACS Appl. Mater. Interfaces*, 2014, **6**, 20535.
24 C. Coughlan, A. Singh and K. M. Ryan, *Chem. Mater.*, 2013, **25**, 653.

25 Y. Shemesh, J. E. Macdonald, G. Menagen and U. Banin, *Angew. Chem., Int. Ed.*, 2011, **50**, 1185.
26 W. Yue, G. Zhang, S. Wang, W. Sun, M. Lan and G. Nie, *Mater. Sci. Semicond. Process.*, 2014, **25**, 337.
27 D. Pan, L. An, Z. Sun, W. Hou, Y. Yang, Z. Yang and Y. Lu, *J. Am. Chem. Soc.*, 2008, **130**, 5620.
28 S. K. Batabyal, L. Tian, N. Venkatram, W. Ji and J. J. Vittal, *J. Phys. Chem. C*, 2009, **113**, 15037.
29 M. Kruszynska, H. Borchert, J. Parisi and J. Kolny-Olesiak, *J. Nanopart. Res.*, 2011, **13**, 5815.
30 X. Shen, E. A. Hernández-Pagán, W. Zhou, Y. S. Puzyrev, J.-C. Idrobo, J. E. Macdonald, S. J. Pennycook and S. T. Pantelides, *Nat. Commun.*, 2014, **5**, 5431.
31 S. Tomic, L. Bernasconi, B. G. Searle and N. M. Harrison, *J. Phys. Chem. C*, 2014, **118**, 14478.
32 C. de Mello Donegá, *Chem. Mater.*, 2015, **27**, 621.
33 S. T. Connor, C.-M. Hsu, B. D. Weil, S. Aloni and Y. Cui, *J. Am. Chem. Soc.*, 2009, **131**, 4962.
34 W.-C. Huang, C.-H. Tseng, S.-H. Chang, H.-Y. Tuan, C.-C. Chiang, L.-M. Lyu and M. H. Huang, *Langmuir*, 2012, **28**, 8496.
35 K. Nose, Y. Soma, T. Omata and S. Otsuka-Yao-Matsuo, *Chem. Mater.*, 2009, **21**, 2607.
36 J. Chang and E. R. Waclawik, *CrystEngComm*, 2013, **15**, 5612.
37 S. T. Connor, C.-M. Hsu, B. D. Weil, S. Aloni and Y. Cui, *J. Am. Chem. Soc.*, 2009, **131**, 4962.
38 J.-Y. Chang and C.-Y. Cheng, *Chem. Commun.*, 2011, **47**, 9089.
39 W. Han, L. Yi, N. Zhao, A. Tang, M. Gao and Z. Tang, *J. Am. Chem. Soc.*, 2008, **130**, 13152.
40 B. Koo, R. N. Patel and B. A. Korgel, *Chem. Mater.*, 2009, **21**, 1962.
41 Z. P. Liu, L. L. Wang, Q. Y. Hao, D. K. Wang, K. B. Tang, M. Zuo and Q. Yang, *CrystEngComm*, 2013, **15**, 7192.
42 V. K. Komarala, C. Xie, Y. Wang, J. Xu and M. Xiao, *J. Appl. Phys.*, 2012, **111**, 124314.
43 Y. Chen, S. Li, L. Huang and D. Pan, *Inorg. Chem.*, 2013, **52**, 7819.
44 M. Jones and G. D. Scholes, *J. Mater. Chem.*, 2010, **20**, 3533.
45 W. Zhang and X. Zhong, *Inorg. Chem.*, 2011, **50**, 4065.
46 L. Li, A. Pandey, D. J. Werder, B. P. Khanal, J. M. Pietryga and V. I. Klimov, *J. Am. Chem. Soc.*, 2011, **133**, 1176.
47 B. J. Wuensch and M. J. Buerger, *Mineral. Soc. Am., Spec. Pap.*, 1963, **1**, 164.
48 H. M. Rietveld, *J. Appl. Crystallogr.*, 1969, **2**, 65.
49 A. C. Larson and R. B. Von Dreele, *Los Alamos National Laboratory Report LAUR*, 1994, 86–748.
50 B. H. Toby, *J. Appl. Crystallogr.*, 2001, **34**, 210.
51 K. Rurack and M. Spieles, *Anal. Chem.*, 2011, **83**, 1232.
52 M. Wojdyr, *J. Appl. Crystallogr.*, 2010, **43**, 1126.
53 B. H. Toby, *Powder Diffr.*, 2006, **21**, 67.
54 X. Lu, Z. Zhuang, Q. Peng and Y. Li, *Chem. Commun.*, 2011, **47**, 3141.
55 J. Tauc, R. Grigorov and A. Vancu, *Phys. Status Solidi*, 1966, **15**, 627.
56 D. Deng, Y. Chen, J. Cao, J. Tian, Z. Qian, S. Achilefu and Y. Gu, *Chem. Mater.*, 2012, **24**, 3029.
57 R. Xie, M. Rutherford and X. Peng, *J. Am. Chem. Soc.*, 2009, **131**, 5691.
58 T. Pons, E. Pic, N. Lequeux, E. Cassette, L. Bezdetnaya, F. Guillemin, F. Marchal and B. Dubertret, *ACS Nano*, 2010, **4**, 2531.
59 A. Weibel, R. Bouchet, F. Boulc'h and P. Knauth, *Chem. Mater.*, 2005, **17**, 2378.
60 M. Ge, C. Guo, L. Liu, B. Zhang and Z. Zhou, *Aust. J. Chem.*, 2009, **62**, 1690.
61 Y. H. Kim, J. H. Lee, D.-W. Shin, S. M. Park, J. S. Moon, J. G. Nam and B. Yoo, *Chem. Commun.*, 2010, **46**, 2292.
62 Y. Xing, H. Zhang, S. Song, J. Feng, Y. Lei, L. Zhao and M. Li, *Chem. Commun.*, 2008, 1476.
63 T. Kino, T. Kuzuya, K. Itoh, K. Sumiyama, T. Wakamatsu and M. Ichidate, *Mater. Trans.*, 2008, **49**, 435.
64 M. J. Turo and J. E. Macdonald, *ACS Nano*, 2014, **8**, 10205.
65 W. Bryks, M. Wette, N. Velez, S.-W. Hsu and A. R. Tao, *J. Am. Chem. Soc.*, 2014, **136**, 6175.
66 P. L. Saldanha, R. Brescia, M. Prato, H. Li, M. Povia, L. Manna and V. Lesnyak, *Chem. Mater.*, 2014, **26**, 1442.
67 T. H. Larsen, M. Sigman, A. Ghezelbash, R. C. Doty and B. A. Korgel, *J. Am. Chem. Soc.*, 2003, **125**, 5638.
68 M. Kruszynska, H. Borchert, A. Bachmatiuk, M. H. Rümmeli, B. Büchner, J. Parisi and J. Kolny-Olesiak, *ACS Nano*, 2012, **6**, 5889.
69 J. J. Ning, K. K. Men, G. J. Xiao, L. Y. Zhao, L. Wang, B. B. Liu and B. Zou, *J. Colloid Interface Sci.*, 2010, **347**, 172.